

Chemically Coupled Fe₂O₃/Graphene Hydrogel as Binder-Free Anode Material for Stable Ni-Fe Battery with High Energy and Power Density

Fuqiang Yin^{+[a]}, Pingping Yang^{+[b]}, Xiaoying Chen,^[b] Qing Yang,^[b] and Jiale Xie*^[b]

Aqueous nickel-iron (Ni–Fe) batteries provide a sustainable solution for large-scale power sources, but their practical applications are still restrained by the nonstable Fe anodes. A simple, inexpensive and mass-manufacturable one-pot strategy is used to in situ grow Fe₂O₃ nanoparticles on graphene sheets for preparing a chemically coupled Fe₂O₃/graphene hydrogel (Fe₂O₃@GH), of which the pore structure can be well rationally tuned by the ratio of graphene to Fe₂O₃. In contrast to the conventional iron oxide/carbon anodes (FeO_x/C), Fe₂O₃@GH anode in Ni–Fe batteries delivers much higher specific capacity (287.2 mAh g⁻¹ vs. 159.5 mAh g⁻¹ at 2 A g⁻¹), better stability

(capacity retention of 95% vs. 61.2% after 1000 charge/discharge cycles) and superior power density comparable with supercapacitors. More remarkably, the assembled full rechargeable Ni–Fe battery made from Ni(OH)₂ microspheres growing on Ni foam (Ni(OH)₂ MSs@NF) (+)//Fe₂O₃@GH (-) achieves excellent cycling stability (retention of 82% of specific capacity after 500 cycles) at a large operating potential of 1.6 V, while delivering the largest energy density of 203 Wh kg⁻¹ and also a highest power density of 6.4 kW kg⁻¹ among the reported full Ni–Fe batteries. This work holds great promises to fabricate alternative safer high-performance vehicle batteries.

1. Introduction

Rechargeable batteries with high power density, high energy density, low cost and long lifetime are of great importance in applications of electrical vehicles and large portable devices.^[1–4] Lithium-ion and lead-acid batteries are currently commercially available for such applications but the former is not cost-effective and the latter suffers greatly from environmental and safety concerns.^[5,6] Traditional aqueous batteries (ABs) are inexpensive and safe, and have attracted greatly growing research interest to elevate their power and energy densities as alternatives for lithium-ion batteries.^[7,8] Different kinds of ABs such as MnO₂/Zn,^[9] LiMn₂O₄/VO₂,^[10] FeF_x/Co(OH)₂,^[11] Ni/Bi,^[12] and Ni/Fe^[13] have been reported. However, many efforts should be devoted to solving the critical issues, such as the severe dendrite growth of Zn,^[14] the poor stability and volume expansion of Bi.^[15] Among them, Ni–Fe ABs possesses some prominent advantages including high energy density (~241.5 mAh g⁻¹), abundant reserve and good recyclability. Nevertheless, their relatively poor iron anode with low energy density and poor stability faces great challenges to be improved for broad practical applications. In view of the

multiple valences (Fe³⁺↔Fe⁰) and rich redox chemistry of iron element in the negative potential window, iron oxides (FeO_x) such as FeO, Fe₂O₃ and Fe₃O₄, possess inexpensive, harmless and environmentally friendly nature, and are promising anode materials for Ni–Fe ABs.^[16,17] However, FeO_x has poor electrical conductivity (~10⁻¹⁴ S cm⁻¹) and bad passivation by iron hydroxide during the discharge process to severely hinder its charge storage capability. To solve this problem, some strategies have been explored to combine FeO_x with carbon-based materials, such as carbon nanotubes, graphene, carbon black, carbon aerogel, etc.^[18–20] For example, graphitic shell wrapped Fe nanoparticles used as iron anode shows a high capacity retention (the initial value of 90%) after 1000 cycles, but only gives a low energy density of 136.7 Wh kg⁻¹.^[21] The FeO_x/reduced graphene oxide (FeO_x/rGO) for an anode shows a high initial capacity (~300 mAh g⁻¹) and a good rate capability, nevertheless, its capacity just retains the initial value of 66.6%.^[22] Molecular confinement iron oxide nanocrystals firmly mounted on carbon (mc-FeO_x/C) served as stable anode material for high energy density Ni–Fe ABs was also reported.^[23] Compared with conventional iron oxide on carbon (FeO_x/C), this mc-FeO_x/C anode exhibits a much higher capacity (370.2 mAh g⁻¹ vs. 159.5 mAh g⁻¹ at 2 A g⁻¹) and better stability (capacity retention of 93.5% vs. 61.2% after 1000 cycles). The mc-FeO_x/C based Ni–Fe battery, meanwhile, delivers high energy density (112.6 Wh kg⁻¹ at 28.9 kW kg⁻¹). Moreover, the slow ion diffusion kinetics of FeO_x electrodes and the blocked fast charge transfer due to the weak interaction between FeO_x and carbon materials are two critical limitations.

Considering that three-dimensional (3D) porous graphene hydrogels (GHs) not only can allow rapid multidimensional electron transfer and accelerate ion diffusion in the network, but also can bring more active sites for the reversible redox

[a] F. Yin⁺
New Energy Vehicle Center
China Automotive Engineering Research Institute Co., Ltd.
Chongqing 401122, China

[b] Dr. P. Yang,⁺ X. Chen, Q. Yang, Dr. J. Xie
Institute of Photovoltaics
Southwest Petroleum University
Chengdu 610500, China
E-mail: jialejie@swpu.edu.cn

[+] These authors contributed equally to this work.

Supporting information for this article is available on the WWW under
<https://doi.org/10.1002/batt.202100289>

reactions without addition of binder and conductive carbon black,^[24] we make efforts to modify FeO_x with GH. Unfortunately, current typical 3D GHs were prepared by chemical reduction of graphene oxide (GO) dispersion, in which toxic organic solvents (DMF, ethylene glycol, methyl alcohol, acetone, acetonitrile, etc.) and toxic reagents ($\text{NH}_3\text{-H}_2\text{O}$, N_2H_4 , etc.) were used to form hydrogels and transform GO into RGO. It is significant to investigate a new way to replace this uneconomical and environmental unfriendly strategy. Therefore, an easy and environmental-friendly approach has been developed for GH synthesis in this work. Moreover, growing the electrochemical active FeO_x directly on conductive graphene sheets as binder free electrodes is very promising.^[25] It can provide the good conductive pathway for FeO_x nanoparticles, utilize the electrochemical activity of FeO_x substantially, and avoid the use of conductive agents in electrode preparation.

Herein, we synthesized 3D macroscopic Fe_2O_3 nanoparticles/graphene hydrogels ($\text{Fe}_2\text{O}_3@\text{GHs}$) by a simple, low-cost, eco-friendly one-pot hydrothermal strategy. Unusually, GO was reduced by Fe^{2+} at high temperature of 200 °C. The as-prepared hybrid hydrogels exhibit a high specific capacity of

304.2 mAh g^{-1} at a current density of 1 A g^{-1} , which is superior to pure Fe_2O_3 powder (97 mAh g^{-1}) and conventional FeO_x/C (287 mAh g^{-1} vs. 159.5 mAh g^{-1} at 2 A g^{-1}). A rechargeable aqueous Ni–Fe battery assembled with Ni(OH)_2 MSs@NF (+)// $\text{Fe}_2\text{O}_3@\text{GH}$ (−) produces an energy density of 203 Wh kg^{-1} and power density of 6.4 kW kg^{-1} as well as remarkable cycling stability with retention of 82% of specific capacity after 500 cycles at a large operating potential of 1.6 V.

2. Results and Discussions

2.1. Material Characterizations

Chemically coupled Fe_2O_3 and graphene hydrogel ($\text{Fe}_2\text{O}_3@\text{GH}$) was prepared from the mixture of Fe^{2+} , GO and $\text{C}_2\text{H}_3\text{O}_2^-$ using a one-pot aqueous hydrothermal process as shown in Figure 1(a). $\text{C}_2\text{H}_3\text{O}_2^-$ is the conjugate base of acetic acid to function as a weak base during the synthesis process, which can also serve as a reductant.^[26] Detailed experimental procedures are given in the experimental section and supporting information (Figure S1). Morphology and structure of the as-synthesized

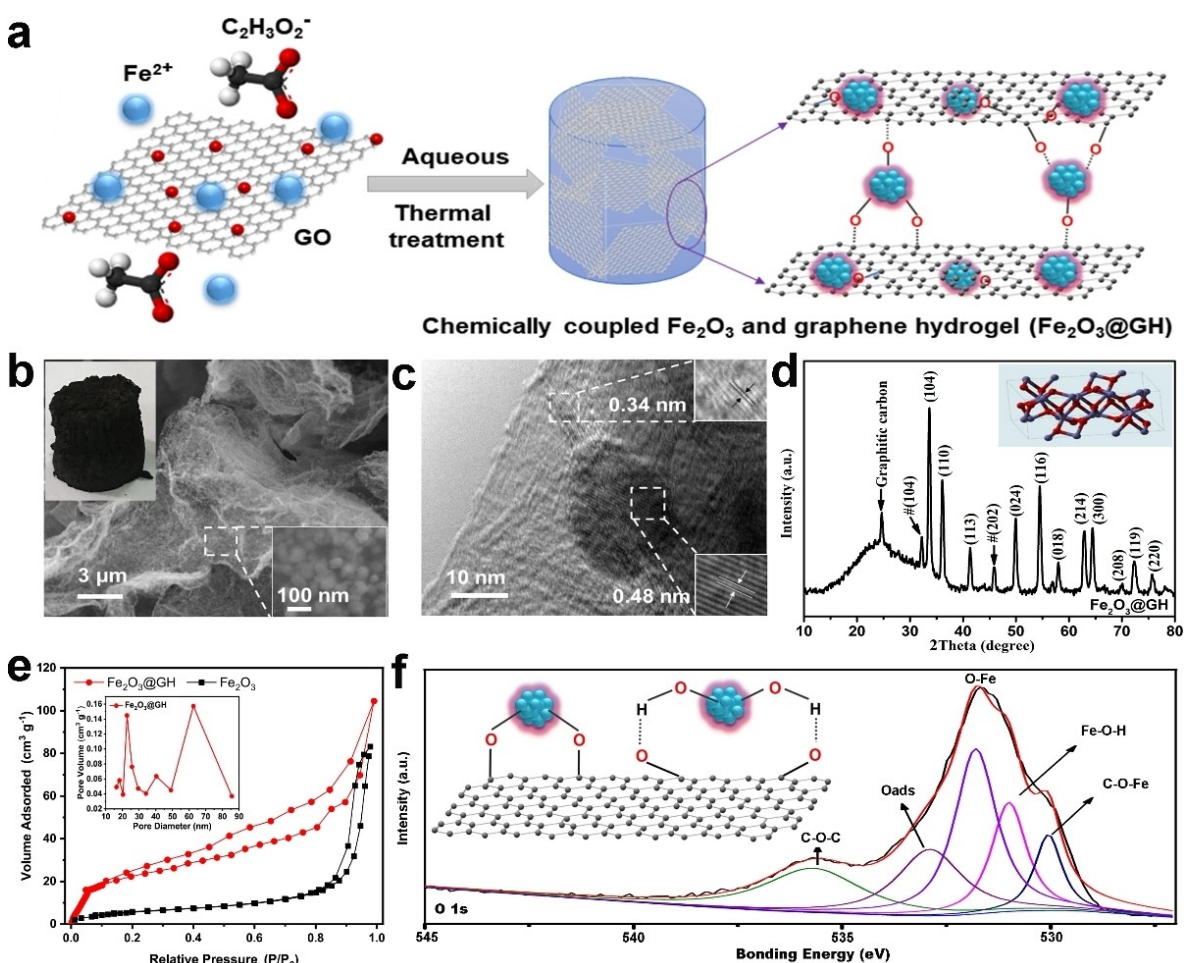


Figure 1. a) Schematic illustration of the fabrication of $\text{Fe}_2\text{O}_3@\text{GH}$. b) SEM image of the $\text{Fe}_2\text{O}_3@\text{GH}$, and the insets are photo of the $\text{Fe}_2\text{O}_3@\text{GH}$ hydrogel and enlarged SEM image. c) TEM image of the $\text{Fe}_2\text{O}_3@\text{GH}$. d) XRD pattern of $\text{Fe}_2\text{O}_3@\text{GH}$, and the crystal structure of Fe_2O_3 . e) Nitrogen adsorption/desorption isotherm and BJH pore size distribution of the $\text{Fe}_2\text{O}_3@\text{GH}$ and Fe_2O_3 . f) XPS O1s spectrum of the $\text{Fe}_2\text{O}_3@\text{GH}$.

material were checked by SEM, TEM and XRD. SEM image in Figure 1(b) clearly shows the uniform distribution of the nanoparticles with an average size of 40 nm on the graphene nanosheets. TEM image in Figure 1(c) reveals that the nanoparticle has a lattice fringe with a spacing of ~ 0.48 nm, which is consistent with that of (012) crystal plane of α -Fe₂O₃. The photographs of various Fe₂O₃@GH hydrogels are shown in Figure S2. During the hydrothermal process, the reduced graphene oxide sheets can self-assemble to form hydrogel through the π - π interaction.^[27] Meanwhile, the water can be encapsulated between the reduced graphene oxide sheets, which can induce the formation of mesopores and macropores after the freeze drying.^[28]

XRD pattern in Figure 1(d) confirms the crystal structure of Fe₂O₃ (JCPDS Card No. 33-0664) as well as a wide peak at around 26° corresponding to graphene, further proving the formation of Fe₂O₃@GH. To explore possible formation mechanism of the Fe₂O₃@GH during the hydrothermal process, a control sample was prepared from a mixture of Fe²⁺ and C₂H₃O₂⁻ using the same procedures as that of the Fe₂O₃@GH but without GO. Instead of Fe₂O₃ nanoparticles as observed for the Fe₂O₃@GH, the control sample is found to be Fe₃O₄ particles with a much larger size in micrometer (Figures S3 and S4). The comparison informs that GO should play as an oxidation agent to promote the formation of Fe₂O₃ as well as a confinement agent to enable the formation of nanoparticles with a much smaller size. After the reaction, GO were reduced to be graphene nanosheets, which cross with each other to form hydrogel, eventually producing Fe₂O₃@GH. The as-fabricated Fe₂O₃@GH has a hierarchical porous structure, as clearly reflected from its nitrogen adsorption/desorption isotherm in Figure 1(e). The distinct hysteresis loop of the isotherm curve exhibits a type IV characteristic, indicating the presence of both mesoporous and macroporous structure.^[29] As calculated from the BJH method, the pores are mainly 20 and 80 nm. The BET specific surface area of Fe₂O₃@GH is $83.05\text{ m}^2\text{ g}^{-1}$, which is much larger than that of plain Fe₂O₃ ($25.18\text{ m}^2\text{ g}^{-1}$), which is favorable in promoting ion diffusion and enhancing active material utilization when to be used in electrochemical testing.

The composition of the Fe₂O₃@GH was determined by EDS, TGA and XPS. The EDS spectrum shows that the material contains elements of C, O and Fe (Figure S5). The TGA curve (Figure S6) displays a weight loss of around 19 wt% during 60 to 460°C , corresponding to the combustion of carbon material in the sample.^[30,31] Therefore, the weight percentage of Fe₂O₃ in the Fe₂O₃@GH is approximate 73 wt%. Moreover, the weight percentage of Fe₂O₃ in the Fe₂O₃@GH can be adjusted by changing the ratio of iron precursor and GO during the hydrothermal synthesis. The electronic structure of the material was investigated by XPS. XPS C1s spectrum (Figure S7a) contains a dominant peak at 284.6 eV for C-C band and two weak peaks at 285.3 and 286.5 eV for oxygen-containing functional groups of C-OH and C-O-C (C=O), respectively, indicating that the GO is successfully reduced to graphene during the reaction process.^[32,33] Moreover, in the XPS C1s spectrum, a peak at around 288.7 eV is also observed, which is believed to be C-O-Fe bond, suggesting the possible presence

of chemically coupled Fe-O-C bond. Fe 2p spectrum (Figure S7b) exhibits two distinct peaks arising at the binding energy of 710.9 and 724.5 eV for respective Fe 2p_{3/2} and Fe 2p_{1/2} with a spin energy separation of 13.6 eV as well as the presence of shake-up satellites at 719.1 and 733.2 eV, which are well consist with the typical fingerprint of Fe₂O₃.^[34,35] XPS O1s spectrum (Figure 1f) can be divided into five peaks, of which the strongest peak at 531.7 eV is assigned to Fe-O in Fe₂O₃ component and the peaks at 532.9 and 535.7 eV for respective O_{ads} (physically adsorbed oxygen) and C-O-C (C=O). The weak peak at 531.2 eV should be related to the Fe-O-H, which might be caused by slight hydrolysis of Fe₂O₃.^[36] More importantly, the peak at 530.6 eV corresponding to C-O-Fe is observed, demonstrating the presence of chemically coupled Fe-O-C bond in the Fe₂O₃@GH.^[34] Raman spectra of Fe₂O₃ and Fe₂O₃@GH are shown in Figure S8. The typical peaks of Fe₂O₃ can be observed at 221, 289, 400, 486, and 658 cm^{-1} , which are related to the A_{1g}, E_g, E_g, A_{1g} and E_g Raman modes, respectively. The D and G characteristic peaks at 1325 cm^{-1} and 1588 cm^{-1} from the reduced graphene can be measured in Fe₂O₃@GH. Intensity ratio values of I_D/I_G for GH, Fe₂O₃@GH-30, and Fe₂O₃@GH-50 are around 1.31, 1.56 and 1.69, respectively. The higher I_D/I_G value of Fe₂O₃@GH indicates that the anchoring of Fe₂O₃ and the elimination of oxygen-containing functional groups on the reduced graphene enhance the defects and structural disorder within the graphene sheets.^[37] This further demonstrates the presence of chemically coupled Fe₂O₃@GH.

2.2. Electrochemical Performance

To evaluate electrochemical performance of Fe₂O₃@GH, electrochemical measurements were carried out in a three-electrode system in 6 M KOH aqueous solution. The CV curves of bare Fe₂O₃ powder, GH and Fe₂O₃@GH at 10 mV s^{-1} are shown in Figure 2(a). It can be seen that GH shows a quasi-rectangle, indicating the nature of electrochemical double-layer capacitive behavior. Differing from graphene hydrogel electrode, both bare Fe₂O₃ electrode and Fe₂O₃@GH electrode clearly exhibit a pair of redox peaks, revealing the Faradaic reaction of Fe(III)/Fe(II). The specific electrochemical reactions during the charge/discharge processes should be same as the reported of Fe₂O₃ grown on the graphene foam and CNTs hybrid films.^[36] By comparison, the integrated area of CV curve of Fe₂O₃@GH electrode is largest among the three materials. Attributing to the synergistic effect of Fe₂O₃ and GH, the Fe₂O₃@GH has super talent to apply to the electrode of Ni-Fe ABs. As shown in Figure 2(b), galvanostatic discharge curves show long discharge platform near -0.8 V , illustrating a typical battery-type behavior and matching well with the CV curves (Figure S9). Notably, the Fe₂O₃@GH gives a specific capacity of 304 mAh g^{-1} at 1 A g^{-1} , even 155 mAh g^{-1} at 10 A g^{-1} for 50.9% retention (Figure S10). The charge curves and Coulombic efficiencies of Fe₂O₃@GH are shown in Figure S11. The Coulombic efficiency increases from 55.8% to 98.0% along with the increasing of current density from 1 to 10 A g^{-1} . Figure 2(c) is the cycling stability of Fe₂O₃@GH at a current density of 2 A g^{-1} , compared

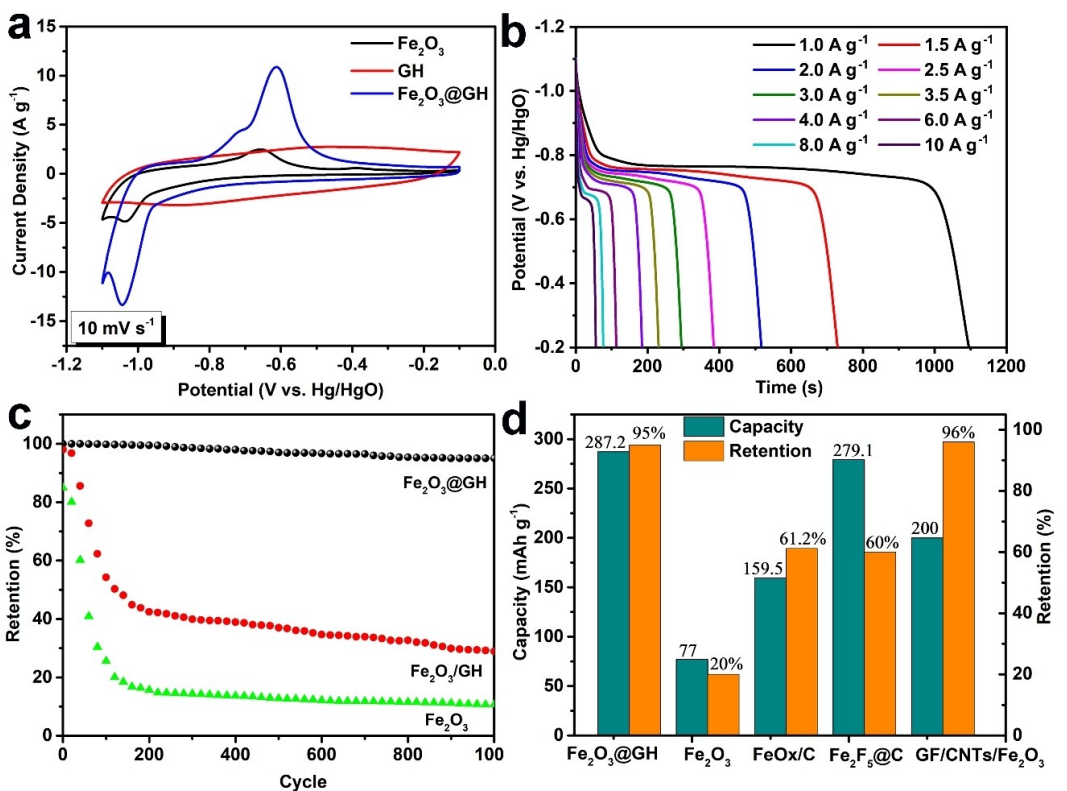


Figure 2. a) CV curves of Fe_2O_3 , GH, and $\text{Fe}_2\text{O}_3@\text{GH}$ at the scan rate of 10 mV s^{-1} . b) GCD discharge curves of $\text{Fe}_2\text{O}_3@\text{GH}$ at the potential window of $-1.1 \sim -0.2 \text{ V}$. c) Cycling performance at 2 A g^{-1} , and d) Bar chart showing the capacities at 2 A g^{-1} and retentions for different iron composites.

with bare Fe_2O_3 and physical mixture of Fe_2O_3 and GH ($\text{Fe}_2\text{O}_3/\text{GH}$). The capacity of bare Fe_2O_3 electrode and $\text{Fe}_2\text{O}_3/\text{GH}$ electrode decline to less than 20% and 30% of initial capacities, respectively, whereas $\text{Fe}_2\text{O}_3@\text{GH}$ electrode still retains $\sim 95\%$ of capacity after 1000 cycles. Figure 2(d) shows bar chart of capacities at 2 A g^{-1} and retentions for different iron composites,^[11,23,36] which demonstrate high capacity and good stability of $\text{Fe}_2\text{O}_3@\text{GH}$. These outstanding electrochemical properties of $\text{Fe}_2\text{O}_3@\text{GH}$, to some extent, could be owed to negligible agglomeration and enhanced interface contact.^[38] The electrochemical performance of $\text{Fe}_2\text{O}_3@\text{GH}$ -20, 30, 40, 50 is shown in Figure S12.

The electrochemical impedance spectroscopy (EIS) is carried out to further evaluate the electrochemical behavior of $\text{Fe}_2\text{O}_3@\text{GH}$ (Figures 3a and S13). It is characterized by a semi-circle in the high frequency region and a straight line in the low frequency region, manifesting a typical diffusion-controlled Warburg behavior. The diameter of the semicircle represents the charge-transfer resistance (R_{ct}) in the redox reaction occurring at the interface of electrode/electrolyte. The equivalent series resistance (R_s) and R_{ct} are estimated to be only ~ 0.51 and $\sim 14 \Omega$, indicating low internal resistance and good conductivity. At the low frequency region, the phase angle of $\sim 60^\circ$ and the low Warburg resistance demonstrate that there is no retarded ionic diffusion phenomena in the test system. The Z' vs. $\omega^{-0.5}$ relationship is plotted in Figure S13(b). The Warburg coefficient σ_ω derived from the slope of above plots is 1.05,

9.75 and $2.33 \Omega \text{ cm}^{-2} \text{ s}^{-0.5}$, corresponding to GH, Fe_2O_3 and $\text{Fe}_2\text{O}_3@\text{GH}$, respectively. Due to the diffusion coefficient $D \propto (\sigma_\omega)^2$,^[39] $\text{Fe}_2\text{O}_3@\text{GH}$ exhibits a great higher D value than that of Fe_2O_3 . This suggests the plenty of pores in $\text{Fe}_2\text{O}_3@\text{GH}$ are critical for the fast mass transport. The contribution of the pseudocapacitive and diffusion-controlled intercalation behavior is further calculated at different scan rates. Figures 3(b) and S14 are the plots of $i(V)/V^{1/2}$ vs. $V^{1/2}$ used for calculating k_1 and k_2 at different potentials, by which CV curve with the pseudocapacitive contribution to the total current can be plotted in Figures 3(c) and S15. It can be observed in Figure 3(d) that the contribution of the pseudocapacitance will augment with the increase of scan rate, since the reaction will transform from diffusion control to surface control at high scan rates and the time for ion diffusion into the host lattices will decrease. In general, it is reliable to employ $\text{Fe}_2\text{O}_3@\text{GH}$ as electrode material in battery systems because of $\text{Fe}_2\text{O}_3@\text{GH}$ giving good conductivity, high specific surface area and favorable pore size distribution. In Figure S16, the morphology of $\text{Fe}_2\text{O}_3@\text{GH}$ after the electrochemical measurements were characterized with SEM. The nanostructures are well maintained although Fe_2O_3 nanoparticles show some aggregations during charge/discharge process.

Naturally, a full aqueous Ni–Fe battery of Ni(OH)_2 MSs@NF (+)// $\text{Fe}_2\text{O}_3@\text{GH}$ (−) is assembled, which is evaluated in 6 M KOH aqueous electrolyte. The device is schematically illustrated in Figure 4(a). CV curves of the anode and the cathode at

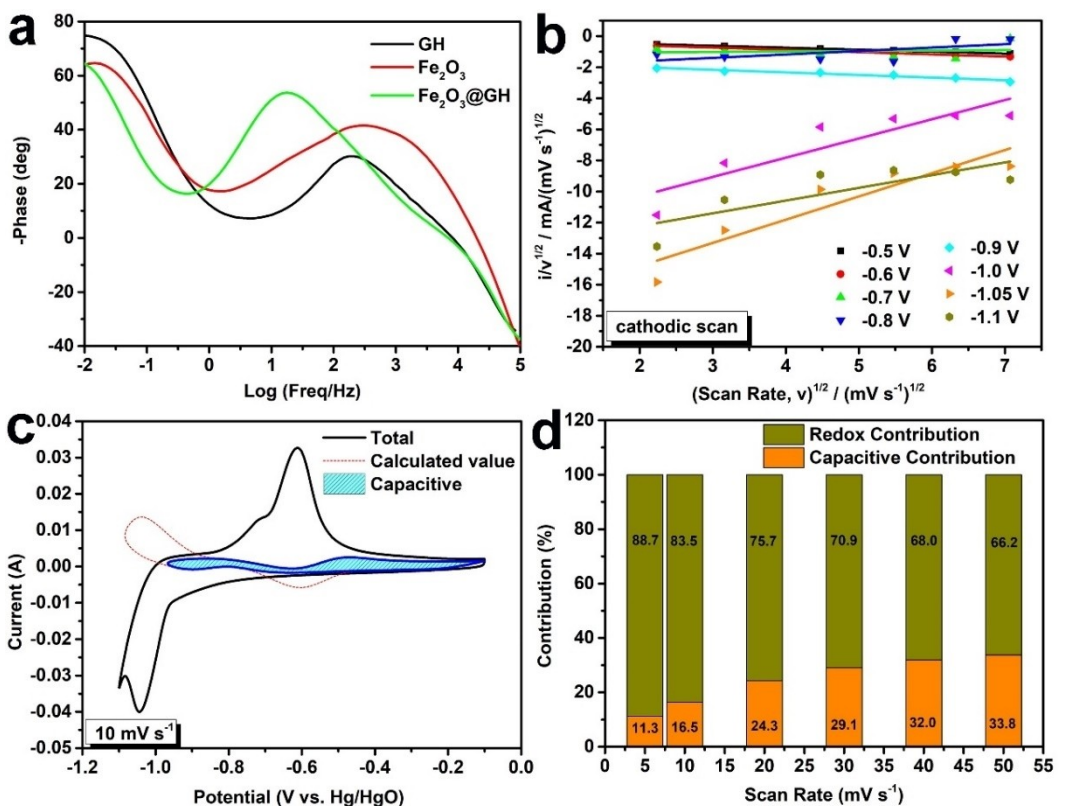


Figure 3. a) Bode plots of GH, Fe₂O₃, and Fe₂O₃@GH in the frequency range of 0.01~100 kHz at the open circuit potential. Electrochemical performance of Fe₂O₃@GH: b) The plots of $i/v^{1/2}$ vs. $v^{1/2}$ used for calculating k_1 and k_2 at different potentials, c) CV curve with the pseudocapacitive contribution to the total current shown by the shaded part at 10 mV s⁻¹, and d) Bar chart showing the fraction of the pseudocapacitive contribution at different scan rates.

20 mV s⁻¹ (Figure 4b) form an exact complementary potential window, which broadens the working voltage of the battery. Figure 4(c) exhibits galvanostatic discharge curves with obvious potential plateau at 1.1 V and a negligible IR drop ($\sim 0.4 \Omega$) at the potential window of 0–1.6 V. Specific capacity of the battery is calculated from GCD curves based on the total mass of Ni(OH)₂ MSs and Fe₂O₃@GH and plotted in Figure S17. The battery outputs a specific capacity of $\sim 127 \text{ mAh g}^{-1}$ at 0.5 Ag⁻¹, which outperform the Ni//mc-FeO_x/C battery (120.2 mAh g⁻¹ at 0.5 Ag⁻¹) and exceeds close to 3 times of magnitude greater than the Ni//FeO_x/C battery (40.5 mAh g⁻¹).^[23] With the current density increased to 1.0, 1.5, 2.0, 2.5, 3.0, 3.5, 4.0 Ag⁻¹, the capacity drops down to 108.2, 88.3, 61.6, 45.1, 36.8, 30.6, and 28.56 mAh g⁻¹, respectively. Ragone plot of Ni(OH)₂ MSs@NF (+)//Fe₂O₃@GH (-) battery is given in Figure 4(d). This device delivers a maximum energy density of 203 Wh kg⁻¹ at power density of $\sim 0.798 \text{ kW kg}^{-1}$ and 92.977 Wh kg⁻¹ at power density of 1.599 kW kg⁻¹. The maximum energy value (203 Wh kg⁻¹) outperform those of recently reported high energy density Ni–Fe battery systems, such as f-Ni/Fe cells (100.7 Wh kg⁻¹),^[36] ultrafast Ni–Fe battery (141 Wh kg⁻¹),^[22] Fe₂O₃/Ni(OH)₂ prototype cell ($\sim 80 \text{ mAh g}^{-1}$),^[40] and mc-FeO_x/C based Ni–Fe battery (173.7 Wh kg⁻¹).^[23] Additionally, the largest power density (6.4 kW kg⁻¹) goes beyond that of thin-film lithium-ion battery and thin-film supercapacitor and comparable to the level of supercapacitors.^[16,24,41–44] To examine the cycling stability of the

Ni–Fe aqueous battery, cycling performance are further performed in Figure 4(e). Gratifyingly, there is less than 18% of capacity fading after 500 cycles under the current density of 2 Ag⁻¹, demonstrating excellent cyclic stability. Finally, three light-emitting diodes (voltage, 1.7–2.3 V) are lighted on by two devices in series (Figure 4f) and light for dozens of minutes, indicating the battery has a potential for practical applications. The cell performance has been compared with the reported Ni–Fe aqueous batteries in Table S1. Ni(OH)₂ MSs@NF (+)//Fe₂O₃@GH (-) device obtains the competitive capacity, stability, energy density, and power density. Moreover, the electrochemical performance of Ni(OH)₂ MSs@NF cathode is shown in Figure S18.

3. Conclusions

In summary, we synthesized 3D macroscopic Fe₂O₃@GH by one-pot hydrothermal method, which is safe, low-cost and eco-friendly. No organic solvents or organic reagents are used during the reduction process of GO and the formation of graphene hydrogel. Owing to the unique structure and superior electric conductivity, the as-prepared Fe₂O₃@GH exhibits excellent electrode performance compared to pure Fe₂O₃, Fe₃O₄, and FeO_x/C. Then, an aqueous battery is assembled based on Ni(OH)₂ MSs@NF as the cathode and Fe₂O₃@GH as the anode.

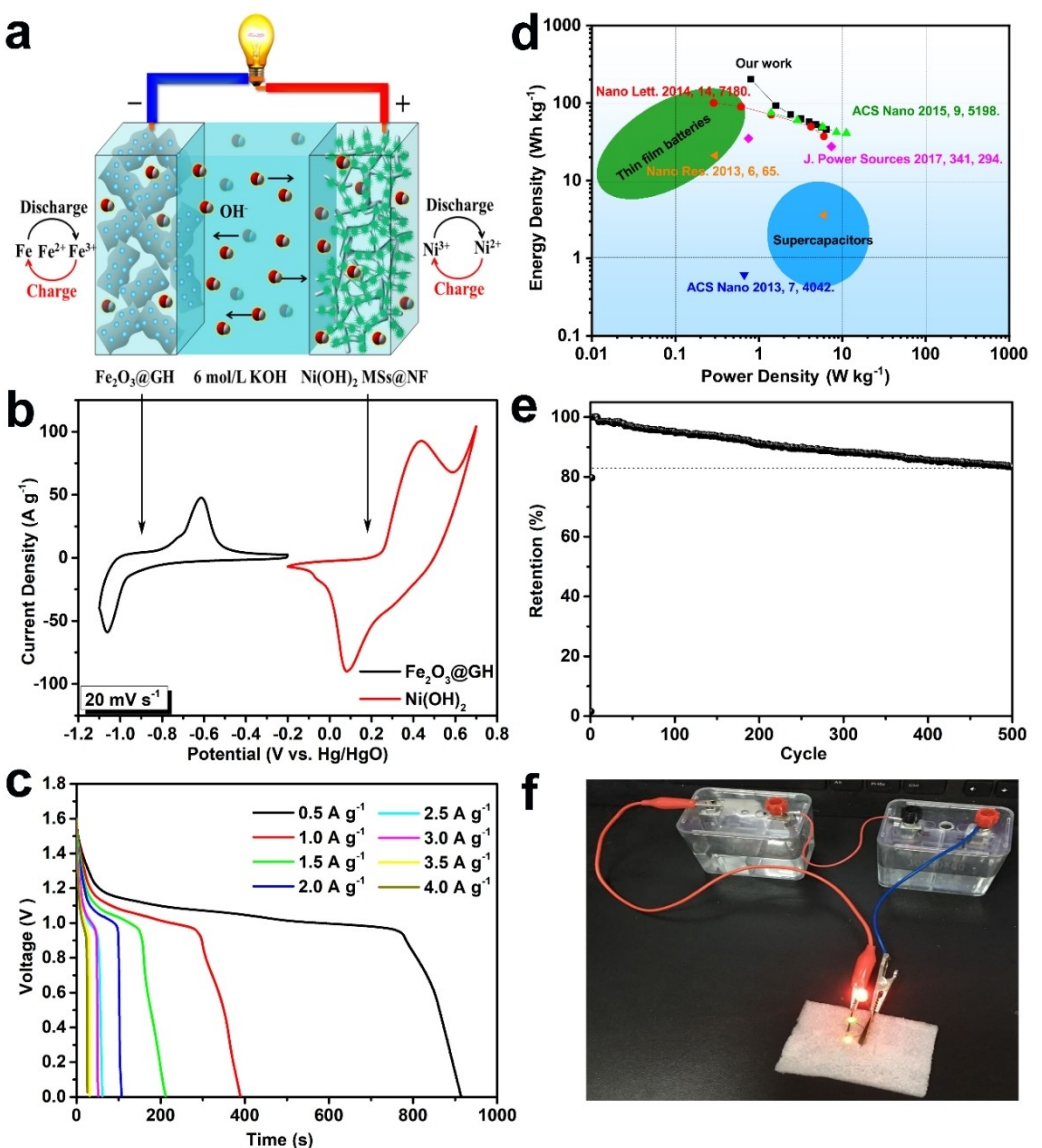


Figure 4. a) Schematic diagram for the full cell of Ni(OH)₂ MSs@NF (+)//Fe₂O₃@GH (-). b) CV curves of Fe₂O₃@GH and Ni(OH)₂ MSs@NF at scan rate of 20 mV s⁻¹. The performance of the full cell: c) GCD discharge curves at the potential window of 0–1.6 V, d) Ragone plots, e) Cycling performance at 2 A g⁻¹, and f) Three light emitting diodes (LED) powered by two serial full cells.

This battery demonstrates a high specific capacity of 127 mAh g⁻¹ at the current density of 0.5 A g⁻¹ and a remarkable cycling stability with 82% specific capacity retention after 500 cycles at a large operating potential of 1.6 V. Besides, it delivers a high energy density of 203 Wh kg⁻¹ along with a power density of 6.4 kW kg⁻¹. The results indicate that this hybrid hydrogel is promising to apply to an aqueous battery, which can probably replace the lithium-ion batteries. This work not only offers a very promising solution for rechargeable aqueous Ni–Fe battery with practical large-scale electric power source applications, but also provides important scientific insight to design an energy storage device with a battery energy density while having a supercapacitor power density.

Experimental Section

Synthesis of 3D Macroscopic Fe₂O₃ Nanoparticles@Graphene Hydrogels

Firstly, 1 mmol FeCl₂·4H₂O was added into 3.8 mL of graphene oxide (GO) dispersion (13.2 mg mL⁻¹) under continuous stirring. The solution was ultrasonicated for 30 min. GO was prepared by an oxidation process of natural graphite powder using the modified Hummers' method. Subsequently, 7 mmol C₂H₃NaO₂·3H₂O was added to the suspension and stirred for another 10 min. Then, the above mixture was transferred into a 50 mL Teflon-line stainless steel autoclave and hydrothermally treated at 200 °C for 6 h. Finally, the obtained monolith (named as Fe₂O₃@GH-50) was immersed in deionized water overnight to remove other impurities. In a similar way, Fe₂O₃@GH-20, Fe₂O₃@GH-30, Fe₂O₃@GH-40 hydrogels were prepared by adjusting the adding of GO. Schematic illustration of the synthesis process and digital photos of Fe₂O₃@GH were shown

in Figures S1 and S2. As a comparison, pure graphene hydrogels (GHs) were prepared via the above method in the absence of $\text{FeCl}_3 \cdot 4\text{H}_2\text{O}$ and $\text{C}_2\text{H}_3\text{NaO}_2 \cdot 3\text{H}_2\text{O}$. In this study, when using the same reactants as those of $\text{Fe}_2\text{O}_3@\text{GH-50}$ except no GO was added by the same hydrothermal procedure, Fe_3O_4 was synthesis instead of Fe_2O_3 , which was distinguished by X-ray powder diffraction (XRD) patterns. The control sample of Fe_2O_3 was prepared by using $\text{FeCl}_3 \cdot 6\text{H}_2\text{O}$ and $\text{C}_2\text{H}_3\text{NaO}_2 \cdot 3\text{H}_2\text{O}$ in absolute ethanol following the same process. FESEM images of Fe_2O_3 and Fe_3O_4 were shown in Figure S3.

Synthesis of Ni(OH)_2 Microspheres on the Ni Foam

A Ni foam (NF, $4.0 \times 2.5 \times 0.25 \text{ cm}^3$) was cleaned with 0.1 M HCl solution and acetone under ultrasonication for 10 min and washed in absolute ethyl alcohol and deionized for three times, successively. Then, a 30 mL mixed aqueous solution containing $\text{NiCl}_2 \cdot 6\text{H}_2\text{O}$ (1.68 mmol), NH_4Cl (3.27 mmol) and $\text{CH}_4\text{N}_2\text{O}$ ($\text{CO}(\text{NH}_2)_2$) (6.66 mmol) was transferred into a 50 mL Teflon-line stainless steel autoclave, following by the NF was dropped into the solution and placed a certain angle against the wall. Hydrothermal growth was carried out at 130°C for 6 h in an electric oven to gain Ni(OH)_2 microspheres directly growing on NF (named as Ni(OH)_2 MSs@NF). Finally, the Ni(OH)_2 MSs@NF was rinsed with deionized water and dried at 80°C for 12 h in ambient air.

Material Characterizations

The morphology of as-prepared products was characterized using a transmission electron microscope (TEM, JEM 2010F) with high resolution and a field emission scanning electron microscope (FESEM, JEOL JSM-7800F) with energy dispersive X-ray spectroscopy (EDS). The crystal structure and surface properties were analyzed by XRD (a Bruker D8 Advance diffractometer using Cu K_α radiation), X-ray photoemission spectrometer (XPS, Thermo Electron, VG ESCALAB 250 spectrometer) and ASAP 2050 Physisorption analyzer (at 77 K). Raman spectra were measured with a Raman spectrometer (Witech, CRM200; 532 nm). Thermogravimetric analysis (TGA) of the samples was done using an SDT600 apparatus at a heating rate of 15 K min^{-1} in air. The mass of electrodes with active materials was measured on a microbalance with an accuracy of 0.01 mg (A&D Company N92, Japan).

Electrode Preparation and Electrochemical Measurements

The 3D macroscopic $\text{Fe}_2\text{O}_3@\text{GH}$ could be directly employed as a working electrode after freeze-drying, in which no polymer or carbon black was added to act as binder or conductor. The well-prepared hybrid hydrogel was cut into rectangular sheets with a dried weight of $\sim 2\text{--}4.0 \text{ mg}$ and pressed between two nickel foams (NF, area: $1.0 \times 1.0 \text{ cm}^2$) to form an electrode under a pressure of $\sim 2 \text{ MPa}$. Testing in this work based on $\text{Fe}_2\text{O}_3@\text{GH-50}$ that was outstanding in $\text{Fe}_2\text{O}_3@\text{GH-20, 30, 40, and 50}$ (Figure S12). Ni(OH)_2 MSs@NF (electrode area: $1.0 \times 1.0 \text{ cm}^2$) was directly employed as another working electrode, whose loading mass ($\sim 3\text{--}4.0 \text{ mg}$) of Ni(OH)_2 was determined by weight differences of NF before and after hydrothermal growth. For the powder materials (Fe_2O_3 , Fe_3O_4), a slurry-coating method was used to prepare the electrodes. The active mass loading on each current collector (NF) was controlled to be $2\text{--}4.0 \text{ mg cm}^{-2}$ to compare with hydrogel electrodes. Electrochemical measurements of single working electrode were carried out in a three-electrode electrochemical cell, with an Hg/HgO as reference electrode and a Pt foil as counter electrode in 6 mol L^{-1} KOH aqueous solution. A CHI 760D electrochemical workstation (CH Instruments Inc., USA) was used to conduct the main electro-

chemical measurements. Each working electrode was immersed into KOH aqueous electrolyte for 30 min before testing and pretreated 5–10 cycles at a rate of 20 mV s^{-1} by cyclic voltammetry (CV) scan. The electrochemical impedance (EIS) measurements was done by applying an AC voltage of 0.005 V amplitude in a frequency range from 0.01 Hz to 100 kHz at open potential and obtaining the Nyquist plots. The full device of aqueous Ni–Fe batteries was assembled with $\text{Fe}_2\text{O}_3@\text{GH}$ anode and Ni(OH)_2 MSs@NF cathode in an optimal ratio of 1:1.5. A 6 mol L^{-1} of KOH aqueous solution saturated with nitrogen gas was used as electrolyte in all electrochemical measurements. The specific capacities (Q_s , mAh g^{-1}) were calculated from galvanostatic discharge curves according to Equation (1):

$$Q_s = \frac{I\Delta t}{3.6m} \quad (1)$$

where I is the discharge current (A), Δt is the discharging time (s), and m is the total active mass of electrodes (g).

The specific energy densities (E , Wh kg^{-1}) and power densities (P , kW kg^{-1}) based on the total active mass of electrodes were estimated by using Equations (2) and (3):

$$E = \int_0^{\Delta t} IV(t)dt \quad (2)$$

$$P = \frac{E}{\Delta t} \quad (3)$$

where I , $V(t)$, dt , Δt are the discharge current (A), the discharge potential window (V), the time differential, and the discharge time (s), respectively.

Supporting Information

Supporting Information is available from the Wiley Online Library or from the author.

Acknowledgements

This work is financially supported by National Natural Science Foundation of China (21703150), the Sichuan Science and Technology Program (2020YJ0123), the Southwest Petroleum University (2019CXTD10) and the Scientific Research Starting Project of SWPU (2021QHZ018).

Conflict of Interest

The authors declare no conflict of interest.

Keywords: aqueous Ni–Fe batteries • binder-free • Fe_2O_3 • graphene hydrogel • rechargeable

- [1] Y. Zhang, L. Tao, C. Xie, D. Wang, Y. Zou, R. Chen, Y. Wang, C. Jia, S. Wang, *Adv. Mater.* **2020**, *32*, 1905923.

- [2] C. Yan, R. Xu, Y. Xiao, J.-F. Ding, L. Xu, B.-Q. Li, J.-Q. Huang, *Adv. Funct. Mater.* **2020**, *30*, 1909887.
- [3] H. Zhang, X. Liu, H. Li, I. Hasa, S. Passerini, *Angew. Chem. Int. Ed.* **2021**, *60*, 598.
- [4] J.-M. Ma, Y.-T. Li, *Rare Met.* **2020**, *39*, 967.
- [5] F. Wu, J. Maier, Y. Yu, *Chem. Soc. Rev.* **2020**, *49*, 1569.
- [6] P. P. Lopes, V. R. Stamenkovic, *Science* **2020**, *369*, 923.
- [7] H. Wang, R. Tan, Z. Yang, Y. Feng, X. Duan, J. Ma, *Adv. Energy Mater.* **2021**, *11*, 2000962.
- [8] H. Tian, Z. Li, G. Feng, Z. Yang, D. Fox, M. Wang, H. Zhou, L. Zhai, A. Kushima, Y. Du, Z. Feng, X. Shan, Y. Yang, *Nat. Commun.* **2021**, *12*, 237.
- [9] M. Manickam, P. Singh, T. B. Issa, S. Thurgate, R. De Marco, *J. Power Sources* **2004**, *130*, 254.
- [10] H. Kim, J. Hong, K.-Y. Park, H. Kim, S.-W. Kim, K. Kang, *Chem. Rev.* **2014**, *114*, 11788.
- [11] J. Jiang, L. Li, M. Xu, J. Zhu, C. M. Li, *ACS Appl. Mater. Interfaces* **2016**, *8*, 3874.
- [12] Q. Li, S. Jing, Z. Yong, Q. Zhang, C. Liu, K. Zhu, Y. Feng, W. Gong, Y. Yao, *Energy Storage Mater.* **2021**, *42*, 815.
- [13] J. Yang, J. Chen, Z. Wang, Z. Wang, Q. Zhang, B. He, T. Zhang, W. Gong, M. Chen, M. Qi, P. Coquet, P. Shum, L. Wei, *ChemElectroChem* **2021**, *8*, 274.
- [14] C. Li, X. Xie, S. Liang, J. Zhou, *Energy Environ.* **2020**, *3*, 146.
- [15] Y. Zeng, Z. Lin, Y. Meng, Y. Wang, M. Yu, X. Lu, Y. Tong, *Adv. Mater.* **2016**, *28*, 9188.
- [16] R. Li, Y. Wang, C. Zhou, C. Wang, X. Ba, Y. Li, X. Huang, J. Liu, *Adv. Funct. Mater.* **2015**, *25*, 5384.
- [17] Q. Li, Q. Zhang, C. Liu, W. Gong, Z. Zhou, P. Man, J. Guo, B. He, K. Zhang, W. Lu, Y. Yao, *Energy Storage Mater.* **2020**, *27*, 316.
- [18] C. Liu, Q. Li, Q. Zhang, B. He, P. Man, Z. Zhou, C. Li, L. Xie, Y. Yao, *Electrochim. Acta* **2020**, *330*, 135247.
- [19] C. Liu, Q. Li, J. Cao, Q. Zhang, P. Man, Z. Zhou, C. Li, Y. Yao, *Sci. Bull.* **2020**, *65*, 812.
- [20] H.-H. Li, A. Saini, R.-Y. Xu, N. Wang, X.-X. Lv, Y.-P. Wang, T. Yang, L. Chen, H.-B. Jiang, *Rare Met.* **2020**, *39*, 1072.
- [21] X. Wu, H. B. Wu, W. Xiong, Z. Le, F. Sun, F. Liu, J. Chen, Z. Zhu, Y. Lu, *Nano Energy* **2016**, *30*, 217.
- [22] H. Wang, Y. Liang, M. Gong, Y. Li, W. Chang, T. Mefford, J. Zhou, J. Wang, T. Regier, F. Wei, H. Dai, *Nat. Commun.* **2012**, *3*, 917.
- [23] C. X. Guo, C. M. Li, *Nano Energy* **2017**, *42*, 166.
- [24] Y. Xu, Z. Lin, X. Huang, Y. Wang, Y. Huang, X. Duan, *Adv. Mater.* **2013**, *25*, 5779.
- [25] Q. Li, Q. Zhang, J. Sun, C. Liu, J. Guo, B. He, Z. Zhou, P. Man, C. Li, L. Xie, Y. Yao, *Adv. Sci.* **2019**, *6*, 1801379.
- [26] X. Zhang, K. Li, H. Li, J. Lu, Q. Fu, Y. Chu, *Synth. Met.* **2014**, *193*, 132.
- [27] H. An, Y. Li, P. Long, Y. Gao, C. Qin, C. Cao, Y. Feng, W. Feng, *J. Power Sources* **2016**, *312*, 146.
- [28] Y. Xu, K. Sheng, C. Li, G. Shi, *ACS Nano* **2010**, *4*, 4324.
- [29] F. Ambroz, T. J. Macdonald, V. Martis, I. P. Parkin, *Small Methods* **2018**, *2*, 1800173.
- [30] P. Mandal, A. P. Chattopadhyay, *Dalton Trans.* **2015**, *44*, 11444.
- [31] J. Jiao, W. Qiu, J. Tang, L. Chen, L. Jing, *Nano Res.* **2016**, *9*, 1256.
- [32] R. Wang, A. Jayakumar, C. Xu, J.-M. Lee, *ACS Sustainable Chem. Eng.* **2016**, *4*, 3736.
- [33] X. Zhou, J. Zhang, H. Wu, H. Yang, J. Zhang, S. Guo, *J. Phys. Chem. C* **2011**, *115*, 11957.
- [34] T. Yamashita, P. Hayes, *Appl. Surf. Sci.* **2008**, *254*, 2441.
- [35] F. Mou, J. Guan, Z. Xiao, Z. Sun, W. Shi, X.-a. Fan, *J. Mater. Chem.* **2011**, *21*, 5414.
- [36] J. Liu, M. Chen, L. Zhang, J. Jiang, J. Yan, Y. Huang, J. Lin, H. J. Fan, Z. X. Shen, *Nano Lett.* **2014**, *14*, 7180.
- [37] Z. Abasali karaj abad, A. Nemat, A. Malek Khachatourian, M. Golmohammadi, *J. Mater. Sci. Mater. Electron.* **2020**, *31*, 14998.
- [38] X. Zhang, S. Li, S. A. El-Khodary, B. Zou, S. Yang, D. H. L. Ng, X. Liu, J. Lian, H. Li, *Nanotechnology* **2020**, *31*, 145404.
- [39] J. Xie, P. Yang, H. He, *J. Electrochem. Soc.* **2016**, *163*, A2203.
- [40] Z. Liu, S. W. Tay, X. Li, *Chem. Commun.* **2011**, *47*, 12473.
- [41] C. Guan, J. Liu, Y. Wang, L. Mao, Z. Fan, Z. Shen, H. Zhang, J. Wang, *ACS Nano* **2015**, *9*, 5198.
- [42] Y. Xu, X. Huang, Z. Lin, X. Zhong, Y. Huang, X. Duan, *Nano Res.* **2013**, *6*, 65.
- [43] X. Yu, B. Lu, Z. Xu, *Adv. Mater.* **2014**, *26*, 1044.
- [44] M. Jin, S.-Y. Lu, L. Ma, M.-Y. Gan, Y. Lei, X.-L. Zhang, G. Fu, P.-S. Yang, M.-F. Yan, *J. Power Sources* **2017**, *341*, 294.

Manuscript received: October 7, 2021

Revised manuscript received: November 5, 2021

Accepted manuscript online: November 15, 2021

Version of record online: November 24, 2021